VTT Technical Research Centre of Finland

Inkjet-Printed Ternary Oxide Dielectric and Doped Interface Layer for Metal-Oxide Thin-Film Transistors with Low Voltage Operation

Gillan, Liam; Li, Shujie; Lahtinen, Jouko; Chang, Chih Hung; Alastalo, Ari; Leppäniemi, Jaakko

Published in:
Advanced Materials Interfaces

DOI:
10.1002/admi.202100728

Published: 23/06/2021

Document Version
Publisher's final version

ADVANCED MATERIALS INTERFACES
www.advmatinterfaces.de

Inkjet-Printed Ternary Oxide Dielectric and Doped Interface Layer for Metal-Oxide Thin-Film Transistors with Low Voltage Operation

Liam Gillan, Shujie Li, Jouko Lahtinen, Chih-Hung Chang, Ari Alastalo, and Jaakko Leppäniemi*

Additive solution process patterning, such as inkjet printing, is desirable for high-throughput roll-to-roll and sheet fabrication environments of electronics manufacturing because it can help to reduce cost by conserving active materials and circumventing multistep processing. This paper reports inkjet printing of $Y_xAl_{2-x}O_3$ gate dielectric, In_2O_3 semiconductor, and a polyethyleneimine-doped In_2O_3 interfacial charge injection layer to achieve a thin-film transistor (TFT) mobility (μ_{sat}) of ≈1 $cm^2 V^{-1} s^{-1}$ at a low 3 V operating voltage. When the dielectric material is annealed at 350 °C, plasma treatment induces low-frequency capacitance instability, leading to overestimation of mobility. On the contrary, films annealed at 500 °C show stable capacitance from 1 MHz down to 0.1 Hz. This result highlights the importance of low-frequency capacitance characterization of solution-processed dielectrics, especially if plasma treatment is applied before subsequent processing steps. This study progresses metal-oxide TFT fabrication toward fully inkjet-printed thin-film electronics.

1. Introduction

Metal-oxide thin-film transistors (TFTs) with flexibility and transparency[1] are enabling applications in flexible, transparent displays.[2] Besides displays, sensing is another key application field for oxide TFTs, including X-ray sensors,[3] photosensors,[4] gas sensors,[5] and biosensors.[6] Compared to their organic counterparts, metal-oxide TFTs can reach better performance, such as higher electron saturation mobility (μ_{sat}) and current density.[7] Oxide TFTs are commonly produced using sequential multistep vacuum and photolithography processes. Solution-process patterning, such as reverse-offset printing,[8] flexographic printing,[9] or inkjet printing[10–13] is desirable for scalable roll-to-roll and sheet-to-sheet fabrication due to reduced cost through high-throughput processing, reducing the number of processing steps and conservation of active materials, which is highlighted for additive inkjet printing.[14] An exemplary application for this technology is displays with inkjet-printed oxide TFT backplanes coupled with inkjet-printed organic light-emitting diode frontplanes.[15,16]

Gate dielectric material has a critical impact on TFT performance. Polarization of charges within the dielectric material occurs upon applied gate bias, which directly influences the extent of charge depletion or accumulation in the semiconductor channel.[17] As TFTs evolve toward smaller architectures with increasingly thinner gate dielectrics, tunneling-related leakage current becomes a limitation with high operation voltages, presenting a need for replacing materials such as SiO_2 ($\varepsilon = 3.9$) with ones having a higher dielectric constant (high-κ).[18]

Binary high-κ oxide dielectrics can be prepared by solution processes.[19,20] Some examples prepared by spin coating or spray pyrolysis include AlO_x ($\varepsilon = 10.4$), ZrO_x ($\varepsilon = 22.6$), YO_x ($\varepsilon = 25.4$), TiO_x ($\varepsilon = 53.4$),[21–23] and LiO_x ($\varepsilon = 6.7$)[24] (ε at 1 kHz). Oxide materials with higher dielectric constant than these examples exist, but those typically possess low bandgaps, making those prone to unfavorable leakage currents.[25] Ternary oxides can provide superior performance compared to binary oxides, by incorporating a high bandgap from one component, combined with a high dielectric constant from another component. Also, by adding a dopant with higher Gibbs free energy of oxidation than the host oxide, one can suppress the

L. Gillan, Dr. A. Alastalo, Dr. J. Leppäniemi
VTT Technical Research Centre of Finland Ltd.
Tietotie 3, Espoo FI-02150, Finland
E-mail: liam.gillan@vtt.fi
S. Li, Prof. C.-H. Chang
School of Chemical
Biological, and Environmental Engineering
Oregon State University
Corvallis, OR 97331, USA
Dr. J. Lahtinen
Department of Applied Physics
Aalto University
Puumiehenkuja 2, Espoo FI-02150, Finland
The ORCID identification number(s) for the author(s) of this article can be found under https://doi.org/10.1002/admi.202100728.

DOI: 10.1002/admi.202100728

low-frequency instability often occurring in solution-processed dielectrics that can lead to the overestimation of charge carrier mobility and device instability.[26] Solution processes have been employed for the generation of ternary oxide dielectrics, including spin coating or spray pyrolysis routes for fabricating $SrTa_2O_6$,[27] $LaAlO_3$,[26,28] $ZrAlO_x$,[29] MgTiO,[30] $HfLaO_x$,[31] $HfSiO_x$,[32] AlNaO,[33] AlPO,[34] and $Y_xAl_{2-x}O_3$.[35,36]

Inkjet printing has been demonstrated for AlO_x[37] and ZrO_2,[38–40] with ZrO_2 also reported via screen printing.[41] Recently, AlO_x was printed by flexography, and far-ultraviolet irradiation was employed to enable annealing at low $T_{ann} \leq 200$ °C.[42] Reports of printed ternary metal-oxide-alloy dielectrics are scarce, and a survey of the literature suggests that they are restricted to inkjet deposition of $YAlO_x$,[17] $Sc_1Zr_1O_x$,[43] and ternary tantalum/aluminum oxide alloys.[44,45] $YAlO_x$ (perhaps better presented as $Y_xAl_{2-x}O_3$) is of particular interest because it exploits Al_2O_3 as the wide bandgap component (≈8 eV), coupled with Y_2O_3 as the high-κ component (ε = 19.8,[35] 25.4[21]). This combined effect provides a material with κ as high as 19.2, greater than that of Al_2O_3 (ε = 11.5).[35] Also, it has been shown that $Y_xAl_{2-x}O_3$ provides lower leakage current density than Al_2O_3 or Y_2O_3.[35] Moreover, as Y has higher Gibbs free energy of oxidation than Al, it could help to enhance the stability of the dielectric at low frequency.[26,46]

In this study, we investigate solution-processed $Y_xAl_{2-x}O_3$ ternary oxide. We demonstrate patterning of the material by inkjet printing, to be used as the dielectric material in In_2O_3 TFTs for low-driving-voltage applications (V_g = 3 V). In addition, building on our previous work,[47] TFT devices were prepared to incorporate a polyethyleneimine (PEI)-doped In_2O_3 interface layer. This interface layer enhances charge injection between the source/drain electrodes and the semiconductor. The inkjet-printed In_2O_3 TFTs with the PEI-doped interface layer exhibit saturation mobility of ≈1 $cm^2\ V^{-1}\ s^{-1}$ at 3 V operation voltage with inkjet-printed $Y_xAl_{2-x}O_3$. In addition, we highlight the importance of measuring the low-frequency capacitance of solution-processed films annealed at low temperature, followed by plasma treatment, to avoid overestimating device mobility.

2. Results and Discussion

2-methoxyethanol (2-ME) has proven to be an effective carrier vehicle for metal-nitrate-based inkjet inks during our previous studies.[48] In this work, we apply the same solvent for $Y_xAl_{2-x}O_3$ precursor ink formulation. To investigate the influence of Y content relative to Al_2O_3, Fourier transform infrared (FTIR) was performed on a sample set prepared by dual layer spin coating of 0.2 M inks with Y:Al ratios of 0, 10, 20, 30, 50, and 100 wt%. Results are presented in Figure S1 (Supporting Information), which reveals that 100 wt% YO_x suffers from large absorption peak signal from around 1800 to 1300 cm^{-1} attributed to H—O—H bending by adsorbed water, and carbonate impurities.[17] Intensity of these absorption signals decreases with reducing Y:Al ratio from 100, 50, 30 to 20 wt%, with the signal appearing similar for both 20 and 10 wt%. This result suggests that up to 20 wt% Y:Al can provide films with low impurities. Subsequently, metal–insulator–metal (MIM) capacitors were prepared from four layers of spin-coated films using inks having a concentration of 0.2 M and Y:Al ratios of 0, 5, 10, and 20 wt%. **Figure 1**a shows how increasing Y wt% reduces the frequency dependence of normalized capacitance to approach the baseline of reference atomic-layer-deposition (ALD)-grown film. In agreement with the data presented in Figure 1a, previous studies by Lee et al.[35] and Bolat et al.[17] have also demonstrated how ≈20 wt% Y loading provides good dielectric properties for application in TFTs. Therefore, 20 wt% Y:Al was selected as the cation atomic ratio for $Y_xAl_{2-x}O_3$ films fabricated during this work. Having identified this suitable composition ratio, gelled ink was subjected to thermal degradation using thermogravimetric analysis (TGA) to pinpoint temperatures for drying (solvent removal) and annealing of spin-coated or printed films. Annealing is required for the removal of impurities and the densification of metal–oxygen–metal structure.[49] The decomposition curve presented in Figure 1b reveals an initial mass loss event of ≈20%, occurring around 120–150 °C, which is assigned to the removal of solvent and organic residues. A second mass loss event is observed around 350–450 °C, with wt% stabilizing at close to 55% by 500 °C, indicating complete

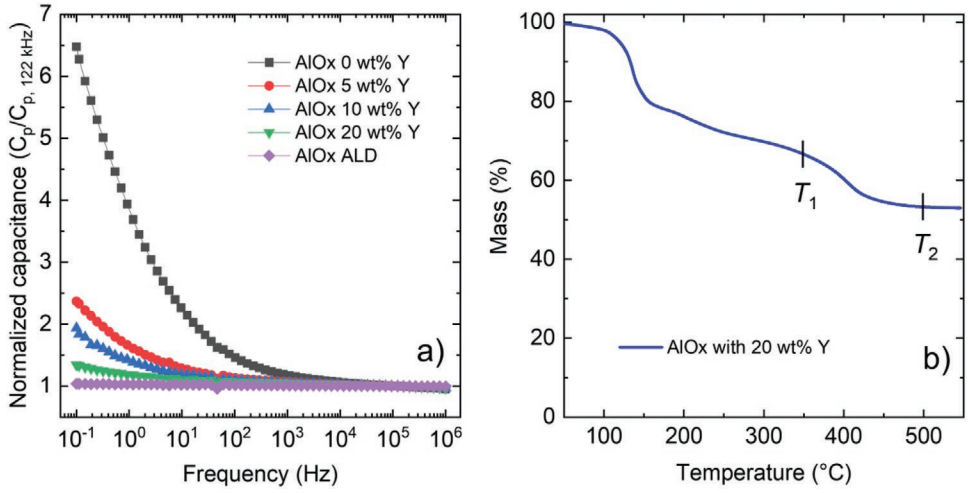

Figure 1. a) Influence of yttrium content on the capacitance of $Y_xAl_{2-x}O_3$ films annealed at 350 °C. b) Thermal gravimetric decomposition plot of gelled $Y_xAl_{2-x}O_3$ precursor ink, annotated with temperatures of 350 °C (T_1) and 500 °C (T_2), for comparison of suitability as annealing temperatures.

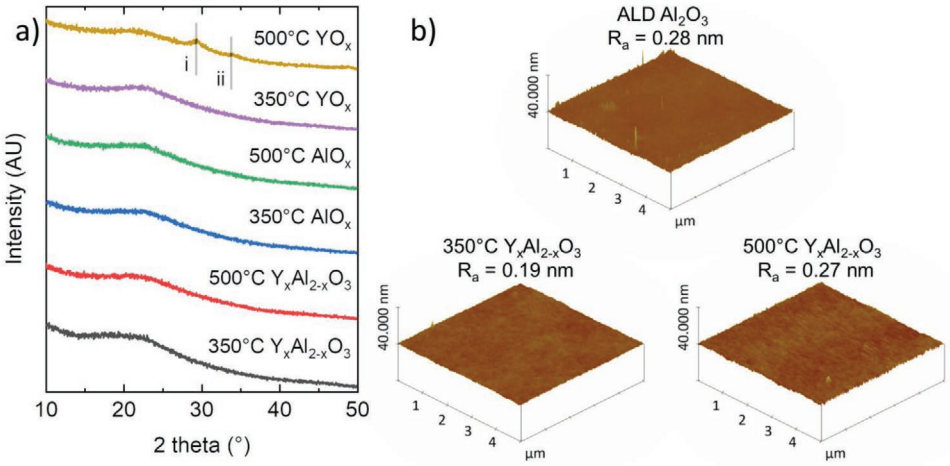

Figure 2. a) X-ray diffraction patterns from spin-coated films (2 × 0.4 M), with a lack of distinct peaks revealing amorphous phase in all cases other than 500 °C YO_x, which possesses minor crystalline peaks at i) ≈29° (222) and ii) ≈34° (400). b) AFM surface profiles of ALD-grown Al_2O_3 and spin-coated (2 × 0.4 M) $Y_xAl_{2-x}O_3$.

conversion of precursors to form the ternary oxide. Based on these TGA data, a drying temperature of 130 °C was selected for solvent removal, and two different annealing temperatures were identified for film characterization investigations. The first annealing temperature (T_1) of 350 °C was selected to probe the electrical performance of the low-temperature-annealed $Y_xAl_{2-x}O_3$ films and the second higher annealing temperature (T_2) of 500 °C, where complete precursor to metal-oxide conversion is expected to have occurred.

Amorphous phase $Y_xAl_{2-x}O_3$ is desired where the material is to be applied as a gate dielectric because polycrystalline films typically suffer from grain-boundary-related problems such as diffusion pathways for impurities,[7] or charge carrier scattering sites, which adversely affect TFT performance including on/off ratio and leakage current.[35] Diffraction patterns from $Y_xAl_{2-x}O_3$ films presented in **Figure 2**a lack the presence of distinct diffraction peaks, possessing only the amorphous halo from silica substrate at 2θ between 15° and 25°. Figure 2a also presents diffraction patterns of solution-processed AlO_x and YO_x films. The AlO_x pattern is concordant with that of the patterns from $Y_xAl_{2-x}O_3$. However, the 500 °C YO_x pattern possesses low intensity (222) and (400) peaks of crystalline YO_x at ≈29° and 34°, respectively.[22] Solution-processed YO_x has been demonstrated as a gate dielectric for TFTs.[22] However, due to suffering from large carbonate impurity at an annealing temperature of 350 °C (Figure S1, Supporting Information) and polycrystallinity at an annealing temperature of 500 °C (Figure 2a), we concluded that the solution-processed pure YO_x is inferior to $Y_xAl_{2-x}O_3$ as a gate dielectric material for TFTs.

Figure 2b presents atomic force microscopy (AFM) analysis of the spin-coated $Y_xAl_{2-x}O_3$ films, with low average roughness (R_a) of 0.19 nm for 350 °C-annealed, and 0.27 nm for 500 °C-annealed films, which is comparable with that of ALD-grown Al_2O_3 (0.28 nm). This smooth dielectric surface is essential for the interface with overlying semiconductor, where a rough surface can introduce charge traps that restrict charge transport in the semiconductor near the dielectric–semiconductor interface.

MIM capacitors were fabricated from two layers of spin-coated 0.4 M $Y_xAl_{2-x}O_3$ ink, with 0.4 M concentration being used to achieve sufficient film thickness with less processing steps required than for the 0.2 M ink. The obtained normalized capacitance (at 122 kHz) for these films annealed at T_1 or T_2 is shown in **Figure 3**a. This result reveals how material annealed at low-temperature T_1 provides stable capacitance across eight orders of magnitude from 10^{-1} to 10^6 Hz, comparable with that of ALD-grown material (Figure 3a). The effect of oxygen plasma treatment was investigated on the capacitors because plasma treatment is generally required in the fabrication of printed oxide TFTs for the removal of contaminant species from the oxide surface, to increase surface energy for providing good wetting of the semiconductor ink, and to facilitate intimate contact at the interface between the printed semiconductor and the dielectric. However, following oxygen plasma treatment, the dielectric annealed at T_1 suffers from frequency dependence, displaying significantly increased capacitance (>10×) below ≈10^2 Hz from the capacitance at high frequency. In contrast to films annealed at T_1, the dielectric film annealed at T_2 does not display frequency dependence in capacitance measurements, even at low frequency and following plasma treatment.

$Y_xAl_{2-x}O_3$ films were characterized using various techniques to understand the low-frequency instability after the plasma treatment. Figure 3b and Figure S2 (Supporting Information) present FTIR spectra both before and after oxygen plasma treatment of spin-coated $Y_xAl_{2-x}O_3$ annealed at either T_1 or T_2, and ALD-grown Al_2O_3, respectively. ALD-grown material and $Y_xAl_{2-x}O_3$ films annealed at T_2 both appear tolerant of plasma treatment. The only observed change is a minor increase in absorption from O—H stretching (3200 to 3650 cm^{-1}) plausibly resulting from surface hydroxylation. On the contrary, $Y_xAl_{2-x}O_3$ film annealed at the lower temperature T_1 is influenced by plasma treatment. In this case, the FTIR spectra present i) strongly increased absorption signal from O—H stretching around 3200 to 3650 cm^{-1} (attributed to surface hydroxylation), ii) the appearance of a minor signal from C—H stretching around 2700 to 2900 cm^{-1} (possibly residual

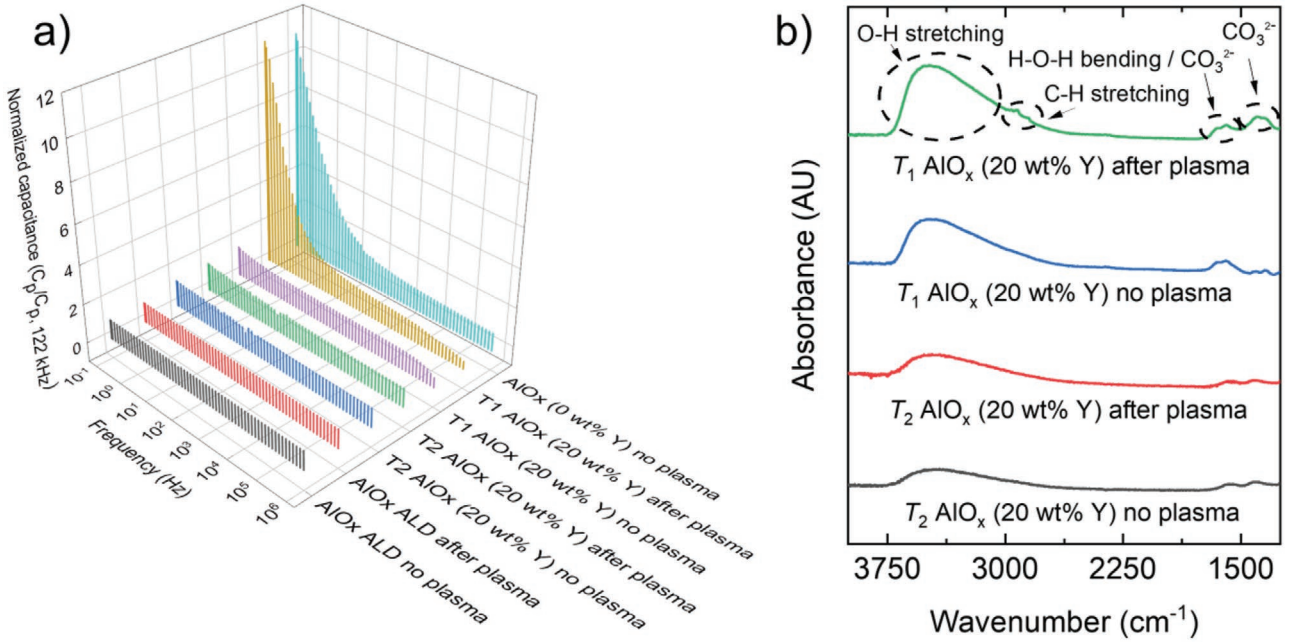

Figure 3. a) Frequency dependence of normalized capacitance, and b) FTIR characterization of spin-coated (2×0.4 M, $T_1 = 350$ °C, $T_2 = 500$ °C) before and after oxygen plasma treatment.

ethylene glycol), and iii) appearance of a significant absorption peak around 1300 to 1500 cm^{-1} residing in the region indicative of carbonate or nitrate species. X-ray photoelectron spectroscopy (XPS) spectra of N 1s/Y 3s region (Figure S3, Supporting Information) showed only the Y 3s peak at ≈394 eV and no evidence of nitrates (above 400 eV).[17,22] Therefore, we assign FTIR signal around 1300–1500 cm^{-1} to carbonate. FTIR signal from H—O—H bending (from adsorbed water) around 1500–1800 cm^{-1} is present for all spin-coated samples before and after plasma treatment.

The FTIR analysis suggests that T_1 is too low of a temperature to properly anneal the solution-deposited dielectric. Plasma treatment may activate and/or degrade residual organic precursors.[50] Another possible explanation for the observed effect of the plasma is that the bulk of $Y_xAl_{2-x}O_3$ films annealed at T_1 remains partially uncured under an overlying crust of more thoroughly cured and densified material. Such high-density top crust has been reported before for solution-processed metal salt precursors both from aqueous[51] and from organic solvent routes (similarly using 2-ME/ethylene glycol (EG) as here).[13] The formation of an interfacial crust is supported by X-ray reflectivity (XRR) data for ALD films and $Y_xAl_{2-x}O_3$ films annealed at T_1 and T_2, as presented in Table S1 and Figures S4 and S5 (Supporting Information). A model with uniform layer density for each layer of the spin-coated multilayer films failed to reproduce the XRR data for T_1 and T_2. By contrast, a model with a nonuniform density for each layer of the multilayer films produced a good fit to the data shown in Figure S4 (Supporting Information). The extracted parameters from the fitting show a higher density crust for each of the layers for both T_1 and T_2 (see Table S1 in the Supporting Information). On the contrary, the ALD-grown reference films are free from such density variations. It has been suggested earlier that such a high-density crust is formed by the enhanced evaporation of the precursor solvent from the top surface. The crust then behaves as a diffusion barrier that prevents the formation of a uniform density gradient in the film.[51]

X-ray photoelectron spectroscopy was performed for insight into the chemical environment of the dielectric films. **Figure 4**a presents C 1s spectra deconvoluted according to positions of components reported for similar materials.[17,35,36] Figure 4a shows that material annealed at 350 °C displays larger carbonate and C=O signal than that of 500 °C-annealed film. Plasma treatment of 350 °C-annealed film results in decreased C=O and increased carbonate signal, with sigma-bonded O—C=O disappearing entirely. The depth profiling of 500 °C-annealed material (C1 s in Figure 4b), shows only adsorbed surface carbon and does not provide evidence for carbon through the bulk of material. By contrast, the depth profiling of 350 °C-annealed material appears to show C—C/C—H and carbonate in the bulk film. The observed carbon in the bulk of the lower temperature annealed films could arise from residual solvents which undergo plasma-induced chemical reaction. TGA (Figure 1b) shows that mass percent has not stabilized at 350 °C. However, the boiling points for ethylene glycol and 2-methoxyethanol are well below the 350 °C annealing temperature at 197 and 124 °C, respectively. An alternative explanation is that the 350 °C-annealed film might be more porous compared with the 500 °C-annealed film. This is supported by XRR data in Table S1 (Supporting Information), which show a higher density for the 500 °C film. C 1s depth profile of plasma-treated 350 °C-annealed film does not show signal for C—C/C—H, but does display pronounced carbonate signal. The yttrium component of the films leads to conversion of adsorbed carbon, such as CO_2, into carbonate.[17] A more porous 350 °C-annealed material would provide a larger surface

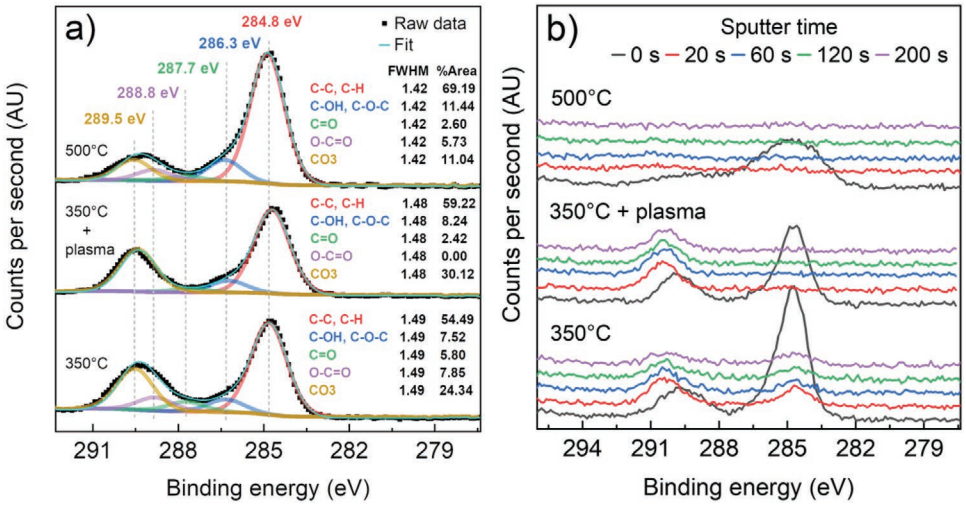

Figure 4. XPS C 1s spectra of 2 × 0.4 M spin-coated $Y_xAl_{2-x}O_3$ films' a) surface and b) depth profiling, sputtered at ≈24 pm s^{-1}.

area for conversion of adsorbates into carbonate, with plasma treatment acting to clean the oxide surface to enhance this process, and/or inducing chemical changes, as supported by large carbonate signal in Figure 4a and disappearance of C—C/C—H signal in Figure 4b. Large surface area of porous film would concurrently result in the generation of large hydroxyl group concentration in response to plasma treatment, as observed in FTIR (Figure 3b). Such a high hydroxyl concentration could explain the low-frequency capacitance instability shown in Figure 3a.[26] Carbonates might also contribute to this instability, but their role in this is not known.

XPS spectra were also recorded at the O 1s region both at the surface and after sputtering. The O 1s area was not peak fitted, because multiple components with close binding energies prevent reliable deconvolution. However, Figure S6 (Supporting Information) presents O 1s spectra annotated with the positions for components reported in analysis of similar materials (see detailed discussion in the Supporting Information).[17,35,36] O 1s spectra in Figure S6a (Supporting Information) show M—O residing in the low binding energy region, and carbon-related signal residing in the high binding energy region of the major O 1s peak. This suggests that the depth profile O 1s shift observed in 350 °C-annealed films (Figure S6b, Supporting Information) could be from increasing percentage of M—O, with a corresponding reduction of carbon impurities. This is supported by decreasing C 1s intensity in depth profile spectra (Figure 4b). In addition, depth profiling of both Al 2p and Y 3d does not present any observed chemical shift throughout the films (Figure S7, Supporting Information). There is no evidence of discrete regions with different chemical environments at varying film depths. This suggests uniform alloying of Y and Al components throughout the oxide films. All XPS sputtering results show signal for 500 °C films at higher binding energies than that of 350 °C films. Charge neutralizer is used in all measurements with the same settings, so charging effects could be responsible for binding energy shift of 500 °C-annealed compared to 350 °C-annealed material.

Although the capacitor annealed at 350 °C shows stable capacitance before O_2 plasma, large O—H and carbonate signal are observed in FTIR (Figure 3), and XPS (Figure 4) reveals high concentration of surface carbonate and presence of carbon through the film bulk. This suggests that 350 °C is insufficient for complete thermal conversion of precursors and densification of $Y_xAl_{2-x}O_3$ films, rendering material annealed at 350 °C unsuitable as a dielectric medium for TFTs. To support this assertion, TFT devices were fabricated using spin-coated $Y_xAl_{2-x}O_3$ at T_1 or T_2, with reference devices employing ALD-grown Al_2O_3. To assist wetting that is required for good printing result and layer uniformity, oxygen plasma was performed on all samples prior to printing of the In_2O_3 semiconductor. The resulting I/V transfer characteristics presented in Figure S8 (Supporting Information) show how devices prepared using ALD Al_2O_3 or $Y_xAl_{2-x}O_3$ at T_2 both exhibit minimal clockwise hysteresis, with the maximum charge carrier saturation mobility (μ_{sat}) of ≈8 and ≈3 $cm^2\ V^{-1}\ s^{-1}$, respectively. However, significant counterclockwise hysteresis occurs from $Y_xAl_{2-x}O_3$ annealed at T_1, in addition to erroneous μ_{sat} of ≈15 $cm^2\ V^{-1}\ s^{-1}$. Here, the capacitance at 20 Hz was used to calculate the mobility from lower frequency I/V transfer measurements. Such underestimation of permittivity can lead to the overestimation of mobility. In accordance with our observations, previous reports suggested that low-temperature solution-processed oxide gate dielectric materials can suffer from increased capacitance at low frequencies due to hydrogen content remaining in the films,[52] for instance, from incomplete sol–gel densification (—M—OH—M—),[26] leading to slow formation/reorientation of dipole moments and/or proton migration upon application of positive gate voltage.[53] Therefore, an annealing temperature of 500 °C was selected for further studies of the material. The results highlight the importance of measuring the low-frequency capacitance after plasma treatment for solution-processed dielectrics, to avoid mobility overestimation in the case that a plasma treatment is performed before the semiconductor film is processed.[26]

Patterning of $Y_xAl_{2-x}O_3$ was realized by inkjet printing, for which the addition of EG cosolvent to the 2-ME-based ink enabled stable droplet formation (Figure S9, Supporting Information), which facilitated well-resolved print patterns in

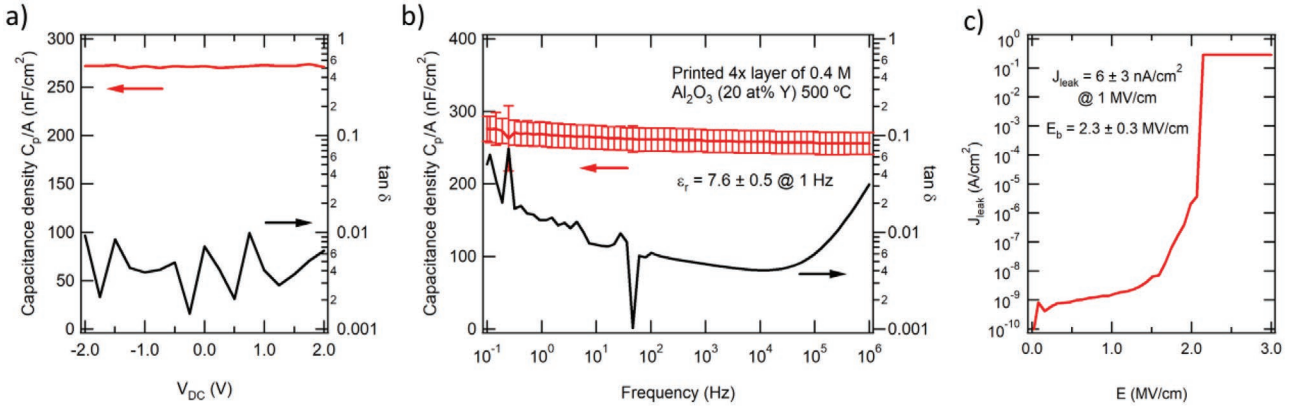

Figure 5. Electrical characterization of inkjet-printed $Y_xAl_{2-x}O_3$ MIM capacitors, depicting capacitance density (C_p/A) and dielectric loss tangent (tanδ) in response to a) the varying voltage at 10 Hz frequency, and b) frequency for 0 V DC and 100 mV AC voltage. c) Electric field influence on leakage current density (J_{leak}).

the generation of films that were ≈20 nm thick (Figure S10, Supporting Information). Four sequential layers were printed to generate the necessary thickness for the dielectric film and to minimize the occurrence of pinhole defects. Fabrication of MIM capacitors incorporating inkjet-patterned $Y_xAl_{2-x}O_3$ enabled the study of the electrical properties of the printed dielectric. **Figure 5**a reveals how capacitance density (C_p/A) is insensitive to direct current voltage (V_{DC}) changes between −2 and +2 V, with the dielectric loss tangent (tanδ) remaining below 0.01 across the same voltage range. In addition, Figure 5b presents C_p/A data where the standard deviation (error bars) across a measured set of 15 MIM devices (15 working devices out of 16 measured devices) affirms the material's insensitivity to frequency across seven orders of magnitude, with tanδ remaining low. These MIM structures are analyzed at 1 Hz, providing a relative permittivity (ε_r) value of 7.6 ± 0.5 for the inkjet-printed $Y_xAl_{2-x}O_3$ material, which is in agreement with an earlier report of inkjet-printed $AlYO_x$ with 20 wt% Y.[17] Gate leakage current density (J_{leak}) plotted as a function of the electric field (E) (Figure 5c) displays a critical breakdown field (E_b) at 2.3 ± 0.3 MV cm^{-1} and low J_{leak} of 6 ± 3 nA cm^{-2} at E = 1 MV cm^{-1}. These metrics are in agreement with data from recent reports of solution-processed Y-doped Al_2O_3 films[17,35] and suggest the suitability of the material as a dielectric medium for oxide TFTs.

We then demonstrated TFTs incorporating $Y_xAl_{2-x}O_3$ film as the gate dielectric with In_2O_3 channel semiconductor and Al gate and source/drain electrodes in bottom-gated devices, as depicted in **Figure 6**. The optical transparency of the oxide constituents renders them challenging to visualize using optical microscopy, even when viewed through a differential interference contrast filter (Figure 6a). Interferometry imaging (Figure 6b) enables visual identification of the oxide films. However, we observe the underlying Al gate electrode generating an artifact of apparent low z-dimension, forming a dark region through the center of the overlying oxides. This observation can be caused by phase ambiguity from the reflective metal surface.[54]

Electrical performance of the printed In_2O_3 TFTs with printed $Y_xAl_{2-x}O_3$ gate dielectric is summarized in column 2 of **Table 1** and in column 5 of Table S2 (Supporting Information), alongside results of other reports for TFTs incorporating solution-processed $Y_xAl_{2-x}O_3$ gate dielectric. **Figure 7** depicts the device architecture and plot of transfer characteristics from representative devices. Overlaid transfer curves for multiple

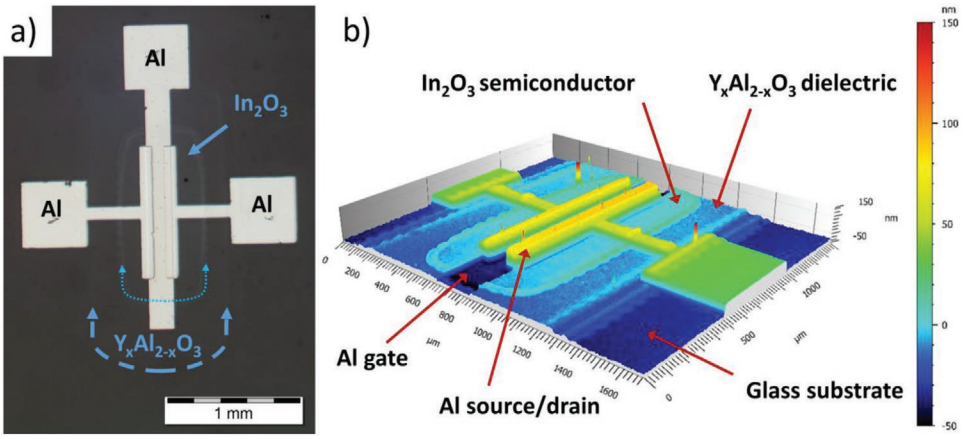

Figure 6. a) Optical microscopy image and b) coherence scanning interferometry profile of TFTs fabricated during this work, revealing the inkjet-printed In_2O_3 and $Y_xAl_{2-x}O_3$ films.

Table 1. Electrical performance metrics of TFTs with three different device architecture combinations of Al source/drain (S/D) electrodes and inkjet-printed 0.1 wt% PEI:InO_x material either absent (column 2), included as a homojunction film (column 3), or employed as an interfacial charge injection layer between semiconductor (SC) and S/D electrodes (column 4). Parameters are hysteresis voltage (V_{hyst}), the maximum drain current ($_{d\ max}$), maximum saturation mobility (μ_{sat}), on/off current ratio ($I_{on/off}$), subthreshold slope (SS), turn-on voltage (V_{on}), and the number of devices of given architecture (n).

Homojunction	–	0.1% PEI:InO_x	–
SC–S/D interlayer	–	–	0.1% PEI:InO_x
V_{hyst} [V]	0.16 ± 0.03	0.20 ± 0.14	0.14 ± 0.02
μ_{sat} [$cm^2\ V^{-1}\ s^{-1}$]	0.41 ± 0.23	1.10 ± 0.54	1.30 ± 0.39
$I_{on/off}$	$3.2 \times 10^4 \pm 6.6 \times 10^4$	$1.1 \times 10^2 \pm 1.3 \times 10^2$	$2.3 \times 10^4 \pm 2.2 \times 10^4$
SS [$V\ dec^{-1}$]	0.44 ± 0.15	1.90 ± 0.73	0.44 ± 0.19
V_{on} [V]	–0.63 ± 0.21	–0.72 ± 0.31	–0.69 ± 0.18
n (TFTs)	15	6	6

devices are provided in Figure S11 (Supporting Information). Table S2 (Supporting Information) reveals that our work is, to the best of our knowledge, the first report of $Y_xAl_{2-x}O_3$ gate dielectric TFTs incorporating more than one printed component. Devices operate with a low voltage range, between –1 and 3 V, with turn-on voltage (V_{on}) close to zero at –0.63 ± 0.21 V and on/off current ratio ($I_{on/off}$) of 10^4. This low voltage operation is essential for the reduction of energy consumption that is critical for applications in flexible and wearable electronics. The maximum charge carrier saturation mobility (μ_{sat}) of 0.41 ± 0.23 $cm^2\ V^{-1}\ s^{-1}$ is in agreement with a previous report with In_2O_3 TFTs with flexographically printed AlO_x dielectric.[42]

Recently, Facchetti and co-workers reported a homojunction of PEI-doped In_2O_3/In_2O_3 as a performance-enhancing channel material for TFTs reliant on Al source/drain (S/D) contacts.[55] In this work, we investigate the effect of an inkjet-printed PEI:InO_x/In_2O_3 homojunction (PEI within the TFT channel), versus PEI:InO_x patterned at the interface between In_2O_3 and Al S/D (PEI interlayer, not within the TFT channel). Well-resolved inkjet patterning of PEI:InO_x material, to avoid deposition within the TFT channel region, requires consideration of PEI loading relative to host oxide. In our earlier work, we found that for concentrations of >0.1 wt% PEI relative to In_2O_3, droplet stabilization proves challenging and leads to poorly defined print resolution.[47] Polymeric species can hinder fluid ejection from inkjet nozzles when present at high concentrations in ink, for example, due to elongational flow in the nozzle, causing viscoelastic stress.[56] For this reason, we employed our previously reported[47] 0.1 wt% PEI:InO_x ink. Upon fabrication of both sets of devices, we observed that

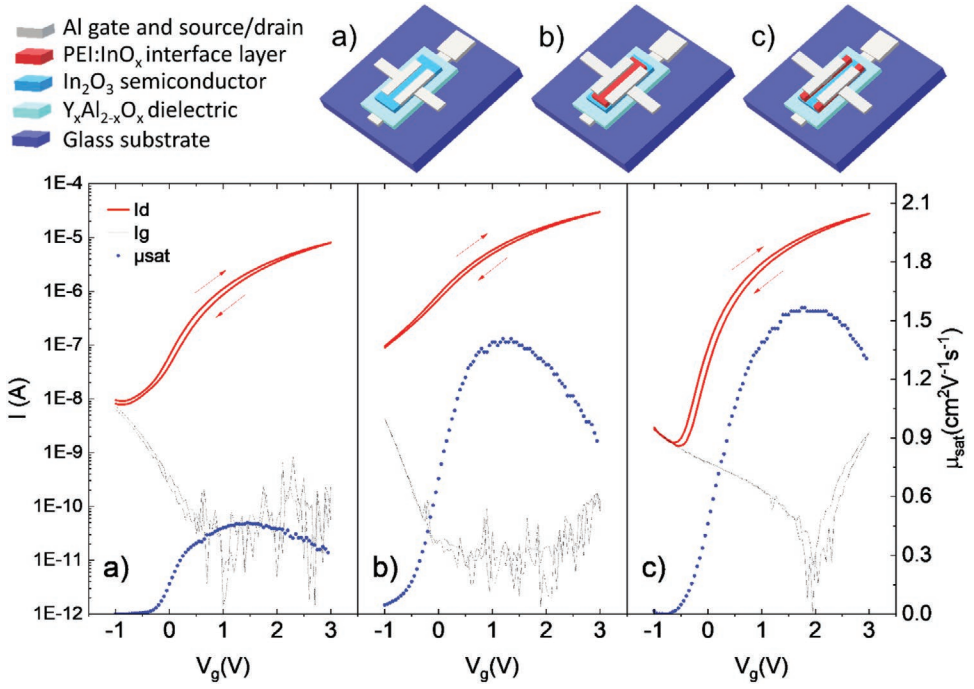

Figure 7. Device architecture and I/V transfer curves of a) primary devices explored during this study, b) devices including a homojunction layer of 0.1 wt% PEI:InO_x, c) devices with 0.1 wt% PEI:InO_x as an interfacial charge injection layer between In_2O_3 semiconductor and Al top contact source/drain electrodes.

in comparison to reference devices devoid of PEI material, those possessing the homojunction (Table 1, column 3 and Figure 7b) showed improved μ_{sat} of 1.10 ± 0.54 cm^2 V^{-1} s^{-1}, however, suffered from the increased subthreshold slope (SS) of 1.90 ± 0.73 V dec^{-1}, and high drain currents with low $I_{on/off}$ of only 10^2 due to increased off-state current. It is plausible that this increased bulk leakage of the semiconductor can occur due to the electron donating ability of PEI, arising from lone pairs of electrons of amine functionality. When PEI material is present in the channel region, these electrons could be available for donation to the conduction band of the host semiconductor oxide, increasing the charge carrier concentration, which leads both to the observed increase in μ_{sat} and I_{off}. This undesirable increase in the semiconductor conductivity was not observed for TFT devices fabricated with patterned PEI:InO_x that was not extending though the entire TFT channel. When comparing the electrical characterization data of reference devices devoid of PEI (Table 1, column 2 and Figure 7a), with that of the patterned PEI interlayer devices (Table 1, column 4 and Figure 7c), it is evident that metrics including V_{hyst}, $I_{on/off}$, SS, and V_{on}, do not significantly deviate from one another. However, there is a clear increase in μ_{sat} from 0.41 ± 0.23 cm^2 V^{-1} s^{-1} for the reference devices, to 1.30 ± 0.39 cm^2 V^{-1} s^{-1} for those with the interfacial PEI:InO_x layer. The electron donating ability of PEI likely assists electron injection across the interface between the oxide semiconductor and the Al contact electrodes, leading to the observed increase in μ_{sat}. In addition, because the PEI material is not present in the device channel, semiconductor conductivity is not increased as was observed for the homojunction devices with high I_{off}, and therefore metrics such as $I_{on/off}$ and SS do not suffer. This is further supported by the output curves presented in Figure S12 (Supporting Information) for devices with each of the three different architectures shown in Figure 7. Notably, the homojunction device in Figure S12b (Supporting Information) suffers from nonsaturating current indicative of bulk leakage, whereas the other devices show saturating currents.[57]

3. Conclusion

We investigated solution-processed $Y_xAl_{2-x}O_3$ dielectric and patterned the material using inkjet printing to fabricate TFT devices incorporating a PEI-doped In_2O_3 interfacial layer, achieving μ_{sat} of ≈1 cm^2 V^{-1} s^{-1} at a low 3 V operating voltage, with 500 °C thermal budget in fabrication. We found that plasma treatment can result in low-frequency capacitance instability if the annealing is not done at high-enough temperature. This result stresses the need to measure the capacitance of solution-processed dielectrics where plasma treatment is applied before subsequent processing steps, to avoid overestimation of charge carrier mobility. Suggested future work includes adapting our previously reported far-ultraviolet treatment[13,42] for lowering the thermal budget of $Y_xAl_{2-x}O_3$ processing, along with the incorporation of printed contacts such as inkjet-printed silver[47] or indium tin oxide.[43] This study advances metal-oxide TFT fabrication toward fully printed devices, which is of importance for scalable, high-throughput production.

4. Experimental Section

$Y_xAl_{2-x}O_3$ precursor inks were prepared under nitrogen atmosphere by adding 2-methoxyethanol (anhydrous, 99.8%, Sigma-Aldrich) to aluminum nitrate hydrate ($Al(NO_3)_3$•$9.8H_2O$, Epivalence UK) or yttrium nitrate hydrate ($Y(NO_3)_3$•$4.1H_2O$, Epivalence UK) in separate vessels, at 0.2 or 0.4 M. Inks were mixed with stirring for 6 h at 75 °C and then filtered via 0.2 µm polytetrafluoroethylene (PTFE), Acrodisc, to obtain a transparent solution. Resulting inks were combined with varying Y:Al ratios of 0, 5, 10, or 20 wt% before adding 10 wt% of ethylene glycol (anhydrous, 99.8%, Sigma-Aldrich). Inks were gelled by heating in an open vessel at 130 °C prior to thermogravimetric analysis that was performed using TA Instruments TGA Q500 at 10 K min^{-1} ramp rate in air. Glass substrates were cleaned sequentially with deionized water, acetone, and isopropanol in an ultrasonic bath at 45 °C. For thin-film material characterization and capacitor structures, spin coating of AlO_x, YO_x, and $Y_xAl_{2-x}O_3$ onto plasma-treated (1 min, 0.2 mbar, O_2, 200 W, Diener Nano) glass substrates (with Al bottom electrode in case of capacitors) at 1500 krpm for 60 s, was followed by hot-plate drying for 15 min at 130 °C. To control film thickness, the spin/drying process was repeated either 2 or 4 times before hot-plate annealing for 30 min in air at either 350 °C (T_1) or 500 °C (T_2). For inkjet printing, $Y_xAl_{2-x}O_3$ ink was mixed for 15 min before filtration (0.2 µm PTFE) into a piezoelectric cartridge (30 °C, DMC-11610) and then printed using a tailored trapezoidal waveform from 14 adjacent nozzles (5 m s^{-1}, 75 µm drop spacing, 339 dpi) with a Fujifilm Dimatix DMP 2831 printer. For both TFTs and capacitors, four sequential layers of $Y_xAl_{2-x}O_3$ were printed onto plasma-treated glass substrates with Al bottom/gate electrode. Each printed layer was hot-plate-dried (15 min, 130 °C), and then all layers jointly annealed (30 min, 500 °C). ALD was employed for the preparation of ≈100 nm thick reference Al_2O_3 films using trimethylaluminum and H_2O as the precursors at 300 °C growth temperature.

Customized shadow masks enabled resistive evaporation patterning of Al as electrical contacts for both capacitors and TFTs. TFTs were fabricated for bottom-gate architecture with inkjet-printed In_2O_3 semiconductor (T_{ann} = 300 °C) and PEI/In_2O_3 composite interfacial layers (T_{ann} = 250 °C), each around 10 nm thick, deposited on top of the inkjet-printed $Y_xAl_{2-x}O_3$ following plasma treatment as previously reported.[13,47] The evaporated Al gate (30 nm) and source/drain electrodes (60 nm) provided a channel length of 80 µm (L) and width (W) of 1 mm (W/L ≈ 12.5). Following the deposition of top contacts, TFTs were hot-plate-annealed in air (150 °C, 30 min) to encourage device turn-on voltage (V_{on}) to approach V_g = 0 V.[9] Capacitor bottom and top contacts were ≈40 and 60 nm thick, respectively.

Attenuated total reflection Fourier transform infrared (ATR-FTIR) spectroscopy (ThermoScientific Nicolet S50i) with grazing angle ATR accessory (Harrick Scientific Products Inc. VariGATR) and Ge crystal was used to obtain FTIR spectra. Grazing incidence X-ray diffraction (GIXRD) (0.5° incidence angle) measurements provided insight into the extent of crystallinity. XRR was used to estimate the density, thickness, and roughness of the multilayer films produced by spin coating. Both GIXRD and XRR were performed using a PANalytical X'Pert PRO MRD with Cu Kα source. The curve fitting for XRR was performed using a software based on the algorithm by Tiilikainen et al.[58] Both single-layer and double-layer models were tested for each layer of the spin-coated multilayer samples using stoichiometric Al_2O_3 as the composition in the fitting. Further insight into film surface morphology was provided by AFM (Digital Instruments, Dimension 3100/Nanoscope 3). Film thickness was verified by stylus profilometry (Veeco, Dektak 150) and optical profiling (Sensofar, S Neox 3D optical profiler, both coherence scanning and phase-shifting interferometry). XPS measurements were made using Kratos Axis Ultra system, equipped with a monochromatic Al Kα X-ray source. The measurements were performed with 100 µm aperture size and 40 eV pass energy (20 eV for Y 3d) with charge neutralizer. XPS depth profiling was performed by making a 2 mm × 2 mm hole on each sample using an Ar-ion gun. The parameters were 5 mA ion current and 5 keV ion energy, resulting in a removal rate of ≈24 pm s^{-1}. Sample surfaces

were measured after 0, 20, 60, 120, and 200 s sputtering durations. XPS surface spectra were binding energy corrected with respect to the adventitious C—C peak at 284.8 eV. In the depth profile measurement data (sputtered to ≈5 nm depth), correction to all spectra was made based on the data before sputtering. All DC electrical characterization was performed with Keithley 4200 SCS in the dark and the capacitance measurements with Novocontrol Alpha-A.

Supporting Information

Supporting Information is available from the Wiley Online Library or from the author.

Acknowledgements

VTT's work was funded in part by the Academy of Finland under Grant Agreement No. 305450 (project ROXI) and No. 328627 (project FLEXRAD). Oregon State University's work was supported by the Walmart Manufacturing Innovation Foundation, Grant #29955421, and the US National Science Foundation, Grant No. CBET 1449383. J.L. performed part of the work while he was a visiting scholar at the Oregon State University. Technical assistance from Pirjo Hakkarainen is gratefully acknowledged. The authors acknowledge the provision of facilities of the Aalto University at OtaNano – Nanomicroscopy Center (Aalto-NMC).

Conflict of Interest

The authors declare no conflict of interest.

Data Availability Statement

Research data are not shared.

Keywords

high-κ oxide dielectrics, inkjet printing, printed electronics, solution-processed oxides, thin-film transistors

Received: May 4, 2021
Published online: May 26, 2021

[1] K. Nomura, H. Ohta, A. Takagi, T. Kamiya, M. Hirano, H. Hosono, *Nature* **2004**, *432*, 488.
[2] Y. Chen, J. Au, P. Kazlas, A. Ritenour, H. Gates, M. McCreary, *Nature* **2003**, *423*, 136.
[3] R. A. Lujan, R. A. Street, *IEEE Electron Device Lett.* **2012**, *33*, 688.
[4] S.-E. Ahn, I. Song, S. Jeon, Y. W. Jeon, Y. Kim, C. Kim, B. Ryu, J.-H. Lee, A. Nathan, S. Lee, G. T. Kim, U.-I. Chung, *Adv. Mater.* **2012**, *24*, 2631.
[5] H. W. Zan, C. H. Li, C. C. Yeh, M. Z. Dai, H. F. Meng, C. C. Tsai, *Appl. Phys. Lett.* **2011**, *98*, 253503.
[6] Y. S. Rim, H. Chen, B. Zhu, S.-H. H. Bae, S. Zhu, P. J. Li, I. C. Wang, Y. Yang, *Adv. Mater. Interfaces* **2017**, *4*, 1700020.
[7] E. Fortunato, P. Barquinha, R. Martins, *Adv. Mater.* **2012**, *24*, 2945.
[8] J. Leppäniemi, A. Sneck, Y. Kusaka, N. Fukuda, A. Alastalo, *Adv. Electron. Mater.* **2019**, *5*, 1900272.
[9] J. Leppäniemi, O. H. Huttunen, H. Majumdar, A. Alastalo, *Adv. Mater.* **2015**, *27*, 7168.
[10] D.-H. Lee, Y.-J. Chang, G. S. Herman, C.-H. Chang, *Adv. Mater.* **2007**, *19*, 843.
[11] D.-H. Lee, S. Y. Han, G. S. Herman, C.-H. Chang, *J. Mater. Chem.* **2009**, *19*, 3135.
[12] S.-Y. Han, D.-H. Lee, G. S. Herman, C.-H. Chang, *J. Disp. Technol.* **2009**, *5*, 520.
[13] J. Leppäniemi, K. Eiroma, H. Majumdar, A. Alastalo, *ACS Appl. Mater. Interfaces* **2017**, *9*, 8774.
[14] W. Xu, H. Li, J.-B. Xu, L. Wang, *ACS Appl. Mater. Interfaces* **2018**, *10*, 25878.
[15] Z. Liu, G. Wang, H. Xie, Z. Wu, Y. Li, C. Jiang, J. Yin, F. Yang, D. Song, G. Yuan, L. Sun, W. Hou, Q. Dai, H. Wang, *SID Int. Symp. Dig. Tech. Pap.* **2013**, *44*, 634.
[16] E. Böhm, P. Levermore, H.-R. Tseng, G. Bealle, H.-J. Wang, P. Hibon, H. Heil, A. Jatsch, H. Buchholz, *SID Int. Symp. Dig. Tech. Pap.* **2017**, *48*, 842.
[17] S. Bolat, P. Fuchs, S. Knobelspies, O. Temel, G. T. Sevilla, E. Gilshtein, C. Andres, I. Shorubalko, Y. Liu, G. Tröster, A. N. Tiwari, Y. E. Romanyuk, *Adv. Electron. Mater.* **2019**, *5*, 1800843.
[18] J. Robertson, *EPJ Appl. Phys.* **2004**, *28*, 265.
[19] S. Park, C. H. Kim, W. J. Lee, S. Sung, M. H. Yoon, *Mater. Sci. Eng., R* **2017**, *114*, 1.
[20] A. Liu, H. Zhu, H. Sun, Y. Xu, Y.-Y. Noh, *Adv. Mater.* **2018**, *30*, 1706364.
[21] W. Xu, H. Wang, L. Ye, J. Xu, *J. Mater. Chem. C* **2014**, *2*, 5389.
[22] A. Liu, G. Liu, H. Zhu, Y. Meng, H. Song, B. Shin, E. Fortunato, R. Martins, F. Shan, *Curr. Appl. Phys.* **2015**, *15*, S75.
[23] G. Adamopoulos, S. Thomas, D. D. C. Bradley, M. A. McLachlan, T. D. Anthopoulos, *Appl. Phys. Lett.* **2011**, *98*, 123503.
[24] A. Liu, G. Liu, C. Zhu, H. Zhu, E. Fortunato, R. Martins, F. Shan, *Adv. Electron. Mater.* **2016**, *2*, 1600140.
[25] K. Yim, Y. Yong, J. Lee, K. Lee, H. H. Nahm, J. Yoo, C. Lee, C. S. Hwang, S. Han, *NPG Asia Mater.* **2015**, *7*, e190.
[26] K. Banger, C. Warwick, J. Lang, K. Broch, J. E. Halpert, J. Socratous, A. Brown, T. Leedham, H. Sirringhaus, *Chem. Sci.* **2016**, *7*, 6337.
[27] L. Lu, Y. Miura, T. Nishida, M. Echizen, Y. Ishikawa, K. Uchiyama, Y. Uraoka, *Jpn. J. Appl. Phys.* **2012**, *51*, 03CB05.
[28] P. N. Plassmeyer, K. Archila, J. F. Wager, C. J. Page, *ACS Appl. Mater. Interfaces* **2015**, *7*, 1678.
[29] W. Yang, K. Song, Y. Jung, S. Jeong, J. Moon, *J. Mater. Chem. C* **2013**, *1*, 4275.
[30] Z. Yang, H. Pu, C. Cui, L. Zhang, C. Dong, Q. Zhang, *IEEE Electron Device Lett.* **2014**, *35*, 557.
[31] J. Ko, J. Kim, S. Y. Park, E. Lee, K. Kim, K. H. Lim, Y. S. Kim, *J. Mater. Chem. C* **2014**, *2*, 1050.
[32] Y. N. Gao, Y. L. Xu, J. G. Lu, J. H. Zhang, X. F. Li, *J. Mater. Chem. C* **2015**, *3*, 11497.
[33] B. N. Pal, B. M. Dhar, K. C. See, H. E. Katz, *Nat. Mater.* **2009**, *8*, 898.
[34] S. T. Meyers, J. T. Anderson, D. Hong, C. M. Hung, J. F. Wager, D. A. Keszler, *Chem. Mater.* **2007**, *19*, 4023.
[35] J. Lee, H. Seul, J. K. Jeong, *J. Alloys Compd.* **2018**, *741*, 1021.
[36] N. Koslowski, V. Trouillet, J. J. Schneider, *J. Mater. Chem. C* **2020**, *8*, 8521.
[37] W. J. Scheideler, M. W. McPhail, R. Kumar, J. Smith, V. Subramanian, *ACS Appl. Mater. Interfaces* **2018**, *10*, 37277.
[38] J. Jang, H. Kang, H. C. N. Chakravarthula, V. Subramanian, J. Jang, H. Kang, V. Subramanian, H. C. N. Chakravarthula, *Adv. Electron. Mater.* **2015**, *1*, 1500086.
[39] Y. Li, L. Lan, S. Sun, Z. Lin, P. Gao, W. Song, E. Song, P. Zhang, J. Peng, *ACS Appl. Mater. Interfaces* **2017**, *9*, 8194.
[40] Z. Zhu, H. Ning, W. Cai, J. Wei, S. Zhou, R. Yao, X. Lu, J. Zhang, Z. Zhou, J. Peng, *Langmuir* **2018**, *34*, 6413.
[41] J. Zhang, X. Li, Y. Gao, *J. Disp. Technol.* **2015**, *11*, 764.
[42] E. Carlos, J. Leppäniemi, A. Sneck, A. Alastalo, J. Deuermeier, R. Branquinho, R. Martins, E. Fortunato, *Adv. Electron. Mater.* **2020**, *6*, 1901071.

[43] Y. Li, L. Lan, S. Hu, P. Gao, X. Dai, P. He, X. Li, J. Peng, *IEEE Trans. Electron Devices* **2019**, *66*, 445.
[44] A. Matavž, R. C. Frunză, A. Drnovšek, V. Bobnar, B. Malič, *J. Mater. Chem. C* **2016**, *4*, 5634.
[45] A. Matavž, B. Malič, V. Bobnar, *J. Appl. Phys.* **2017**, *122*, 214102.
[46] K. K. Banger, R. L. Peterson, K. Mori, Y. Yamashita, T. Leedham, H. Sirringhaus, *Chem. Mater.* **2014**, *26*, 1195.
[47] L. Gillan, J. Leppäniemi, K. Eiroma, H. Majumdar, A. Alastalo, *J. Mater. Chem. C* **2018**, *6*, 3220.
[48] J. H. Leppäniemi, K. Ojanperä, T. Kololuoma, O. H. Huttunen, J. Dahl, M. Tuominen, P. Laukkanen, H. Majumdar, A. Alastalo, *Appl. Phys. Lett.* **2014**, *105*, 113514.
[49] S. Jeong, J. Moon, *J. Mater. Chem.* **2012**, *22*, 1243.
[50] J. Friedrich, W. Unger, A. Lippitz, S. Geng, I. Koprinarov, G. Kühn, S. Weidner, *Surf. Coat. Technol.* **1998**, *98*, 1132.
[51] K. C. Fairley, D. R. Merrill, K. N. Woods, J. Ditto, C. Xu, R. P. Oleksak, T. Gustafsson, D. W. Johnson, E. L. Garfunkel, G. S. Herman, D. C. Johnson, C. J. Page, *ACS Appl. Mater. Interfaces* **2016**, *8*, 667.
[52] X. Zhuang, S. Patel, C. Zhang, B. Wang, Y. Chen, H. Liu, V. P. Dravid, J. Yu, Y. Y. Hu, W. Huang, A. Facchetti, T. J. Marks, *J. Am. Chem. Soc.* **2020**, *142*, 12440.
[53] X. Liang, L. Liu, G. Cai, P. Yang, Y. Pei, C. Liu, *J. Phys. Chem. Lett.* **2020**, *11*, 2765.
[54] Q. Vo, F. Fang, X. Zhang, H. Gao, *Appl. Opt.* **2017**, *56*, 8174.
[55] Y. Chen, W. Huang, V. K. Sangwan, B. Wang, L. Zeng, G. Wang, Y. Huang, Z. Lu, M. J. Bedzyk, M. C. Hersam, T. J. Marks, A. Facchetti, *Adv. Mater.* **2019**, *31*, 1805082.
[56] B.-J. de Gans, E. Kazancioglu, W. Meyer, U. S. Schubert, *Macromol. Rapid Commun.* **2004**, *25*, 292.
[57] D. Hong, G. Yerubandi, H. Q. Chiang, M. C. Spiegelberg, J. F. Wager, *Crit. Rev. Solid State Mater. Sci.* **2008**, *33*, 101.
[58] J. Tiilikainen, J.-M. Tilli, V. Bosund, M. Mattila, T. Hakkarainen, V.-M. Airaksinen, H. Lipsanen, *J. Phys. D: Appl. Phys.* **2007**, *40*, 215.